Journal of Low Temperature Physics (2018) 193:1206–1213
https://doi.org/10.1007/s10909-018-2073-2

Optimizing Thermal Detectors for Low-Threshold Applications in Neutrino and Dark Matter Experiments

N. Bastidon[1] · J. Billard[2] · E. Figueroa-Feliciano[1] · S. Heine[3] · Z. Hong[1] · H. D. Pinckney[1]

Received: 6 November 2017 / Accepted: 28 September 2018 / Published online: 6 October 2018

Abstract
Nuclear recoil detectors with low energy thresholds of 10–100 eV have applications in both neutrino physics (e.g. coherent elastic neutrino-nucleus scattering and neutrinoless double beta decay) as well as for $\mathcal{O}$(GeV)-mass dark matter searches. Cryogenic crystal detectors are well suited for these applications, although some require very large masses which can be achieved with arrays of these detectors. An optimization of a design focusing on ease of fabrication and mass production while retaining low energy thresholds is presented. This is achieved by decoupling the complex lithography of the thermal sensor from the large crystal absorber/target, while optimizing the thermal time constants to retain the lowest threshold possible.

Keywords Transition-edge sensor · Sterile neutrino · Cryogenic detector · Coherent elastic neutrino-nucleus scattering

1 Introduction

The study of coherent elastic neutrino-nucleus scattering (CEνNS) [1,2] has various applications including the research of non-standard neutrino interactions [3,4], sterile neutrinos [5,6], reactor monitoring [7,8], and are a background to $\mathcal{O}$(GeV) dark matter searches [9–11]. The recent 6.7 σ discovery of coherent neutrino-nucleus scattering by the COHERENT collaboration at Oak Ridge National Laboratory made these studies even more promising [12]. Several groups [13–15] are focusing on the detection of

✉ N. Bastidon
noemie.bastidon@northwestern.edu

1 Department of Physics and Astronomy, Northwestern University, Evanston, IL 60201, USA

2 IPNL CNRS, Villeurbanne 69622, France

3 Kavli Institute MIT, Cambridge, MA 02109, USA

CEνNS using cryogenic crystal detectors. Very similar techniques have been widely used in neutrinoless double beta decay searches ($0\nu\beta\beta$) [16,17].

Cryogenic crystal detectors have been used in dark matter searches using athermal readout where ballistic, non-thermalized phonons are collected on the surface of the crystal (e.g. SuperCDMS [18]). Recently, single-electron–hole pair resolution using Luke–Neganov amplification has been demonstrated using an athermal readout [19]. Other experiments (e.g. EDELWEISS [20], CRESST [21], CUORE [17]) have used cryogenic crystals in a thermal mode where the phonon signal is sensed after it has reached thermal equilibrium in the absorber.

When designing future neutrino experiments, there are several trade-offs to be considered. CEνNS detection requires a low threshold which depends on the energy of the neutrinos in question. For reactor neutrinos, thresholds of $\mathcal{O}$(100 eV) are required, whereas for neutrinos from electron capture sources, the necessary thresholds are $\mathcal{O}$(10 eV) [5]. For $0\nu\beta\beta$ decay, low thresholds are important to reject pileup events that can degrade the signal in the region of interest.

For many of these experiments, a large mass $\mathcal{O}$(100–1000 kg) is required. These masses are reached by making arrays of detectors, making the cost per detector and the ability to mass produce them important variables in the overall design. In this paper, we focus on a design that is optimized for low threshold and mass production, by separating the complex thermal sensor from the massive crystal absorber/target, as proposed in [22]. In this way, standard wafer lithography can be used to mass produce thousands of small thermometers which are then coupled to their respective crystal absorber/target. This design is one of many options for future neutrino experiments, and although it trades off some threshold sensitivity, the advantages in mass production make it an interesting direction to research. As presented in [22], this design is also interesting for $0\nu\beta\beta$ decay searches, although that application is not the focus of this paper.

If one wants to separate the thermometer from the target, a thermal design is a natural choice. Incoming neutrinos, photons, betas or dark matter will scatter against the nucleus from a crystal target. The small increase in temperature produced by such an event will be measured by a transition-edge sensor (TES) device that resides on a small chip attached to the target. This will result in a change in resistance and current that will be read out by a superconducting quantum interference device (SQUID) through inductive coupling. Such design is flexible and allows for various target materials to be used depending on the application. Possible materials include zinc, germanium and silicon for neutrino studies and germanium, silicon, sodium iodide and gallium arsenide for dark matter search [22]. Ge- and Si-based detectors are radiopure materials, while Zn crystal could enable pulse-shape discrimination between nuclear and electron recoils [15].

The preliminary design that has been considered for this thermal study includes a 1-cm^3 silicon crystal and a 0.04-mm^2 tungsten TES deposited on a silicon wafer (see Fig. 1). The TES chip has dimensions of 2 mm $\times$ 4 mm and is thermally connected to the target through a gold wire bond to a gold pad on the target. This gold pad is sized to have a fast electron-phonon time constant to allow the TES to quickly enter thermal equilibrium with the target [22]. The aimed transition temperature is of 20 mK with a

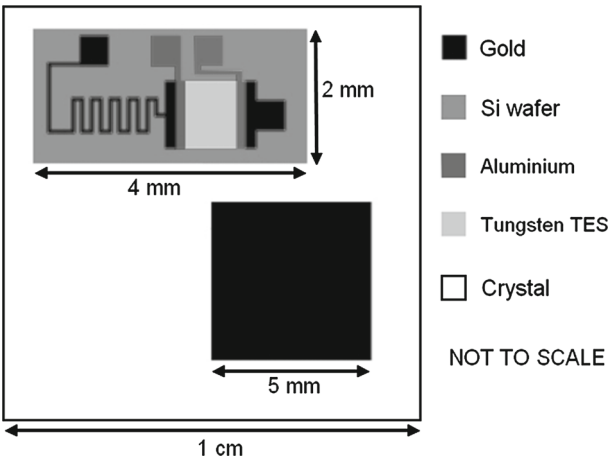

Fig. 1 Preliminary design view from the top. The target crystal is represented in *white*. The parts made of gold are depicted in *black*. The tungsten TES is in *light grey*, while the aluminium pads are in *dark grey* and the Si wafer is of a *medium grey* colour. Note that although not visible in this top view, the TES extends below the aluminium which leads to overlap with the gold pads to attain good thermal contact

TES normal resistance of 1 Ω. The device would be operated in a cryostat with a bath temperature of 10 mK.

2 Thermal Model

In order to simulate the intrinsic properties of the thermal detector considered here, a thermal model based on a block diagram has been built (see Fig. 2) [22–24]. Every block corresponds to one of the elements constituting the device and is characterized by a heat capacity C (see Table 1) and a temperature T. They are connected via thermal links with distinct conductances G (see Table 1). The heat capacities and thermal conductances are calculated from bulk values for the different materials. In this model, we do not include Kapitza resistances [25], which could become important in some cases and will be included in future work. The main place where Kapitza could play a role is between the target and its gold pad, but due to its large size we expect it to be a sub-dominant term in the thermal conductance (see Table 1). We also neglect athermal phonon dynamics, as we assume that the thermalization time across the gold pad to the TES is slower than the athermal time constant. Since a faster time constant between the target and the TES leads to better energy resolution, neglecting athermal phonons is a conservative choice.

As described in [24], we deduce from this thermal diagram a set of ordinary differential equations expressing the changes in current for the electrical circuit as well as the variation in temperature for every entity. This results in a matrix of $N+1$ equations (N being the number of elements in the diagram).

Linear and nonlinear solvers have been used to solve the system of equations in order to compute the noise-equivalent power (NEP), the energy resolution, as well as the sensor response to energy depositions. In the preliminary design, the target material

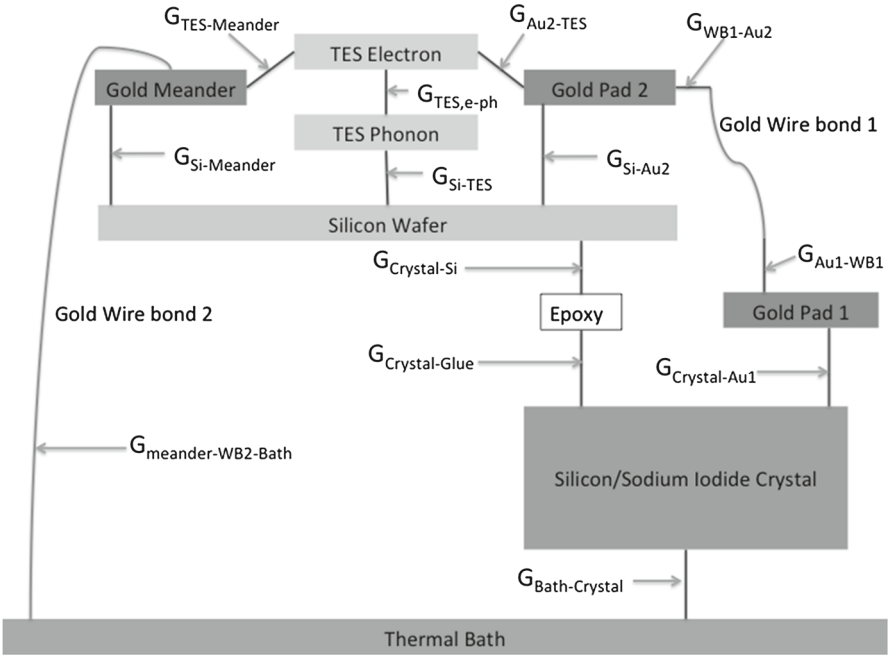

Fig. 2 Block diagram of the preliminary model—an energy input is applied to a crystal target (*silicon/sodium iodide crystal*). The temperature will increase in the connected gold pad (*gold pad* 1) that will then transmit the heat through a gold wire bond (*gold wire bond* 1) to a gold pad deposited on the silicon wafer (*gold pad* 2). This flowing energy will be absorbed by the TES electron system, resulting in a change in resistance in the TES electrical circuit. The thermalized system will then slowly cool down thanks to a gold meander connected to the bath by a gold wire bond (*gold wire bond* 2). The epoxy plays a mechanical role. Kapitza resistance has not been included in this model

modelled was silicon connected to a tungsten TES. For a 100 eV energy input into the crystal, an energy resolution of approximately 5 eV and a decay time of 3 ms have been obtained.

The TES phonon system was not included in the model as it has negligible effects on the overall results and its small heat capacity compared to the other parts of the thermal system introduces convergence problems in the nonlinear solver. We also assume the conductance from mechanical supports of the target crystal can be made negligible compared to the meander design conductance by the use of teflon or other low-conductivity supports, so $G_{\mathrm{Bath-Crystal}}$ has been set to zero for this study.

One problem that was raised very early in the optimization process concerns the epoxy attaching the TES chip to the target crystal. This feature has two drawbacks. The first one is connected to its heat capacity. Indeed, the heat capacity of the glue could be large at cryogenic temperatures. The second one is the possibility of the glue thermal conductance being high enough to allow a significant fraction of the heat deposited in the target material to flow into the TES silicon chip through the epoxy instead of flowing to the TES through the gold pad. However, a test was performed where the thermal conductance of the gluing material was tuned in a range of 16 orders of magnitude resulting in a tenth of an eV resolution changed. The metal/wire bond

Table 1 On the *left*, heat capacities and volumes of each of the preliminary model components

Component	Heat capacity	Volume	Conductances
Si crystal	5.5×10^{-12} J/K	1 cm^3	$G_{Bath-Crystal} \simeq 0$ W/K
Epoxy (Stycast 1266)	1.3×10^{-11} J/K	0.2 mm^3	$G_{Crystal-Au1} = 7.7 \times 10^{-8}$ W/K
Gold pad 1	4.3×10^{-11} J/K	5 mm × 5 mm × 250 nm	$G_{Crystal-Glue} = 2.1 \times 10^{-7}$ W/K
Si wafer	1.6×10^{-14} J/K	2 mm × 4 mm × 375 μm	$G_{Crystal-Si} = 2.1 \times 10^{-7}$ W/K
Gold wire bond 1	1.4×10^{-11} J/K	50 μm diam. 5 mm long	$G_{Au1-WB1} = 7.0 \times 10^{-6}$ W/K
Gold pad 2	5.6×10^{-14} J/K	0.25 mm × 0.25 mm × 600 nm	$G_{WB1-Au2} = 7.0 \times 10^{-6}$ W/K
TES phonon system	7.0×10^{-19} J/K	0.2 mm × 0.2 mm × 600 nm	$G_{Si-Au2} = 9.6 \times 10^{-11}$ W/K
TES electron system	5.1×10^{-14} J/K	0.2 mm × 0.2 mm × 600 nm	$G_{TES,e-ph} = 6.1 \times 10^{-12}$ W/K
Gold meander	3.8×10^{-14} J/K	600 nm thick 5 μm wide 8.9 mm long	$G_{Au2-TES} = 5.3 \times 10^{-6}$ W/K
Gold wire bond 2 (20 mK)	1.4×10^{-11} J/K	50 μm diam. 5 mm long	$G_{TES-Meander} = 1.7 \times 10^{-5}$ W/K
			$G_{Si-Meander} = 6.8 \times 10^{-11}$ W/K
			$G_{Meander-WB2} = 3.0 \times 10^{-9}$ W/K
			$G_{WB2-Bath} = 3.5 \times 10^{-6}$ W/K

On the *right*, conductances of the thermal links. The thermal conductance from the silicon wafer to the TES phonon system is not included as it is in series with the much smaller TES electron–phonon conductance. Additionally, this thermal conductance will likely be dominated by the Kapitza resistance

conductivity between the target and the TES always dominates the heat flow, so the thermal conductance of the glue ends up being negligible.

The second issue of such a design is mechanical. The epoxy will contract and expand in various ways during the cool-down process, risking breaking the target crystal. A possible solution is to replace the epoxy with a silicon oil [26] which will allow the crystal and wafer to move freely during the cool-down without breaking, as such a material solidifies only below a given temperature. Other solutions are presented in [27,28].

3 Preliminary Design Variations

In a first step, variations of the preliminary design have been considered. Two different TES recipes have been studied in this simulation work: W [29] and Au–Ir–Au [30].

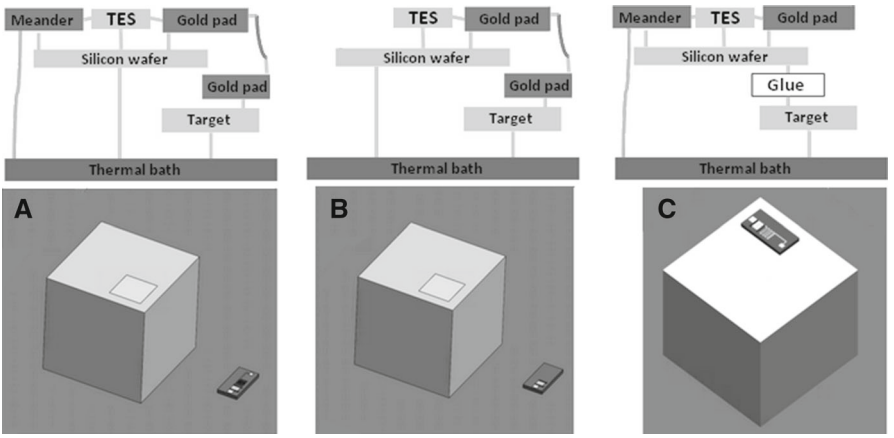

Fig. 3 Three model variations—in *design A* and *B*, the silicon wafer is sitting on the bath. In *design A*, the TES is connected to the bath through a gold meander. Glue is used in *design C*. In addition, the TES is connected to the bath through a gold meander

Table 2 Results obtained for some variations of the preliminary design with a $T_c = 20$ mK

Target thickness	Si target, W TES	NaI target, W TES	Zn target, W TES	Si target, Au–Ir–Au TES
1 cm	1.4 eV	13.5 eV	4 eV	1.4 eV
4 mm	1.0 eV	–	–	1.0 eV

All resolutions are optimized for a 10 ms decay time (i.e. the length of the meander and the surface of the gold pad 2 are tuned to give the optimal resolution when the decay time is 10 ms). The 10 ms decay time has been chosen arbitrarily and serves as a benchmark. Weights are given for a few crystals: 1 cm^3 Si is 2.3 g, 1 cm^3 NaI is 3.7 g and 1 cm^3 Zn is 7.1 g

The two different TESs have given very similar results. In addition, several crystal materials have been considered: Si, Zn and NaI. Silicon and zinc are two materials being considered for neutrino applications by our collaborators, while the sodium iodide would be used for a dark matter application, similar to [31]. The lower heat capacity of silicon is responsible for the better resolution results. Results obtained for Zn and NaI are not taking into consideration specific processes such as superconductivity for Zn and scintillation for the NaI. Numbers are then only given as a thermal estimation. Finally, two different crystal sizes have been considered for the silicon target case: 1 cm^3 and 4 mm $\times$ 1 cm^2. Results are summarized in Table 2.

The optimization process of the thermal chip has been done iteratively, where each element geometry's influence has been studied. This resulted in three new additional designs, each bringing their own pros and cons (see Fig. 3).

One of the priorities has been to remove the silicon oil from the model. Two different solutions based on the same principle are proposed. The solutions involve placing the TES silicon chip off the target, connected to the cold bath. The thermal connection is then made through a simple gold wire bond going from the target's gold pad to the silicon wafer's gold pad. The thermal connection between the TES silicon chip and the

Table 3 On the *left*, heat capacities and volumes of each of the model components given for the optimized design C with tungsten TES and 1 cm^3 Si crystal

Component	Heat capacity	Volume	Conductances
Si crystal	5.2×10^{-12} J/K	1 cm^3	$G_{Bath-Crystal} \simeq 0$ W/K
Polydimethylsiloxane (PDMS)	7.1×10^{-15} J/K	0.2 mm^3	$G_{Crystal-PDMS} = 2.1 \times 10^{-7}$ W/K
Si wafer	1.5×10^{-14} J/K	2 mm × 4 mm × 375 μm	$G_{Si-Au2} = 4.7 \times 10^{-10}$ W/K
Gold pad 2	2.6×10^{-13} J/K	162 μm × 1.9 mm × 600 nm	$G_{Si-TES} = 6.1 \times 10^{-12}$ W/K
TES W	5.1×10^{-14} J/K	0.2 mm × 0.2 mm × 600 nm	$G_{Au2-TES} = 6.3 \times 10^{-5}$ W/K
Gold meander	1.4×10^{-12} J/K	600 nm thick 5μm wide 247 mm long	$G_{TES-Meander} = 1.7 \times 10^{-5}$ W/K
Gold wire bond 2 (10 mK)	7.0×10^{-12} J/K	50 μm diam. 5 mm long	$G_{Si-Meander} = 5.0 \times 10^{-9}$ W/K
			$G_{Meander-WB2} = 2.1 \times 10^{-11}$ W/K
			$G_{WB2-Bath} = 1.7 \times 10^{-6}$ W/K

On the *right*, conductances of the thermal links. Note that in this model there is no dedicated phonon system. G_{Si-TES} is the electron–phonon conductance. Polydimethylsiloxane is a component of silicone oil

bath is made either by the gold meander and a gold wire bond to the bath (i.e. design A) or by simply relying on the conductance of the silicon chip itself (i.e. design B).

All of these designs are not optimal to work with a material such as sodium iodide as they require depositing a gold pad directly on the hydrophilic target. Indeed, such crystals are extremely sensitive to their environment. Modification processes are extremely complicated and often result in permanent damage [32]. The third proposed design (i.e. design C) would solve this issue by avoiding the deposition of gold. In this case, silicon oil could be used to connect the target to the wafer. Its conductance would be the only path for the heat absorbed by the target and would then not act as a parasitic conductance.

This simulation study shows that the silicon target devices are extremely promising with both W and Au–Ir–Au TESs (see Table 2). The resolutions achieved were between 1.3 and 2.5 eV for Si target design A to C (see Table 3). Experimental studies of these various detector geometries will allow to test more in details their specifications.

4 Conclusion

A preliminary thermal detector model including a crystal target and a TES has been optimized through numerical simulation, resulting in a series of four possible detector

geometries. Every device has its own pros and cons concerning ease of implementation and fabrication as well as energy resolution characteristics. We have designed a mask set with devices based on this work and will be testing them in the following months.

Acknowledgements DP has been supported by the Northwestern University and the Illinois Space Grant Consortium. GNU paralell has been used to perform this analysis [33].

References

1. D.Z. Freedman, Phys. Rev. D **9**, 1389 (1974). https://doi.org/10.1103/PhysRevD.9.1389
2. K. Scholberg, J. Phys. Conf. Ser. **606**, 012010 (2015)
3. M. Abdullah, J.B. Dent, B. Dutta, G.L. Kane, S. Liao, L.E. Strigari (2018). arXiv:1803.01224
4. D.K. Papoulias, T.S. Kosmas, Phys. Rev. D **97**, 033003 (2018). https://doi.org/10.1103/PhysRevD.97.033003
5. J.A. Formaggio, E. Figueroa-Feliciano, A.J. Anderson, Phys. Rev. D **85**, 013009 (2012). https://doi.org/10.1103/PhysRevD.85.013009
6. B. Dutta, Phys. Rev. D **94**, 093002 (2016). https://doi.org/10.1103/PhysRevD.94.093002
7. P.S. Barbeau, J.I. Collar, J. Miyamoto, I. Shipsey, IEEE Trans. Nucl. Sci. **50**, 5 (2003). https://doi.org/10.1109/TNS.2003.818237
8. C. Hagmann, A. Bernstein, IEEE Trans. Nucl. Sci. **51**, 5 (2004). https://doi.org/10.1109/TNS.2004.836061
9. R. Essig, M. Sholapurkar, T. Yu (2018). ArXiv eprint arXiV:1801.10159
10. B. Dutta, S. Liao, L.E. Strigari, J.W. Walker, Phys. Lett. B **773**, 242 (2017). https://doi.org/10.1016/j.physletb.2017.08.031
11. F. Ruppin, J. Billard, E. Figueroa-Feliciano, L. Strigari, Phys. Rev. D **90**, 083510 (2014). https://doi.org/10.1103/PhysRevD.90.083510
12. D. Akimov, Science **357**, 6356 (2017). https://doi.org/10.1126/science.aao0990
13. R. Strauss, Eur. Phys. J. C **77**, 8 (2017). https://doi.org/10.1140/epjc/s10052-017-5068-2
14. G. Agnolet, Nucl. Instrum. Methods Phys. Res. A **853**, 53 (2016). https://doi.org/10.1016/j.nima.2017.02.024
15. J. Billard, J. Phys. G Nucl. Part. Phys. **44**, 105101 (2017)
16. G.B. Kim, Astropart. Phys. **91**, 105 (2017). https://doi.org/10.1016/j.astropartphys.2017.02.009
17. C. Alduino, Phys. Rev. Lett. **120**, 132501 (2018). arXiv:1710.07459
18. R. Agnese, Phys. Rev. D **95**, 082002 (2017). https://doi.org/10.1103/PhysRevD.95.082002
19. R.K. Romani, Appl. Phys. Lett. **112**, 043501 (2018). https://doi.org/10.1063/1.5010699
20. E. Armengaud, J. Instrum. **12**, 08 (2017). https://doi.org/10.1088/1748-0221/12/08/P08010
21. M. Kiefer, Opt. Mater. **31**, 10 (2009). https://doi.org/10.1016/j.optmat.2008.09.019
22. M. Pyle, E. Figueroa-Feliciano, B. Sadoulet (2015). arXiv:1503.01200v2
23. F. Proebst, J. Low Temp. Phys. **100**, 1–2 (1995). https://doi.org/10.1007/BF00753837
24. E. Figueroa-Feliciano, J. Appl. Phys. **99**, 114513 (2006). https://doi.org/10.1063/1.2191449
25. P.L. Kapitza, J. Phys. USSR **4**, 181 (1941)
26. G. Angloher, Eur. Phys. J. C **76**, 441 (2016). https://doi.org/10.1140/epjc/s10052-016-4278-3
27. M. Kiefer, AIP Conf. Proc. **1185**, 651 (2009). https://doi.org/10.1063/1.3292426
28. R. Strauss, Nucl. Instrum. Methods A **845**, 414–417 (2017). https://doi.org/10.1016/j.nima.2016.06.060
29. R. Agnese, Phys. Rev. Lett. **116**, 071301 (2016). https://doi.org/10.1103/PhysRevLett.116.071301
30. G. Wang, IEEE Trans. Appl. Supercond. **24**, 4 (2015). https://doi.org/10.1109/TASC.2016.2646373
31. F. Reindl et al. (2017). ArXiv preprint arXiv:1711.01482
32. A. Hubbard. Doctoral dissertation. The University of Wisconsin-Madison (2015)
33. 0. Tange, GNU paralell—the command-line power tool. USENIX Mag. **36**, 1 (2011). https://doi.org/10.5281/zenodo.16303